



Article

Deuteration Effects on the Transport Properties of $(\text{TMTTF})_2\text{X}$ Salts

Andrea Rohwer ^{1,*}, Martin Dressel ^{1,*}  and Toshikazu Nakamura ² 

¹ 1. Physikalisches Institut, Universität Stuttgart, Pfaffenwaldring 57, 70569 Stuttgart, Germany; andrea.rohwer@pi1.physik.uni-stuttgart.de

² Institute for Molecular Science, Myodaiji, Okazaki 444-8585, Japan; t-nk@ims.ac.jp

* Correspondence: dressel@pi1.physik.uni-stuttgart.de; Tel.: +49-711-685-64946

Received: 20 October 2020; Accepted: 24 November 2020; Published: 27 November 2020



Abstract: The electronic properties in the quasi-one-dimensional Fabre salts are strongly affected by electronic correlations along the molecular stacks, but also by the interactions with the anions located in a cage that is formed by the methyl end groups. We systematically compare the charge transport in deuterated and protonated $(\text{TMTTF})_2\text{X}$ salts with the anions $\text{X} = \text{Br}, \text{PF}_6, \text{SbF}_6,$ and ClO_4 , ranging from Mott and Efros–Shklovskii variable-range hopping to activated band transport with a temperature dependent energy gap. The strong dependence of charge localization and ordering on the anion size and deuteration confirms the subtle structural involvement of the anions in the charge transport along the TMTTF stack.

Keywords: charge-transfer salts; $(\text{TMTTF})_2\text{X}$; deuteration; anions; charge transport

1. Introduction

Fascinated by the wealth of exciting physical phenomena summarized in the temperature-pressure phase landscape plotted in Figure 1, the Fabre salts $(\text{TMTTF})_2\text{X}$ —here TMTTF denotes tetramethyl-tetrathiafulvalene and X is a monovalent anion—have been intensely investigated since their discovery in the 1970s [1–3].

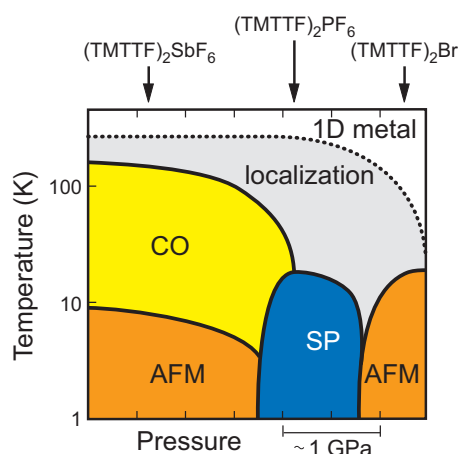


Figure 1. Phase diagram of the $(\text{TMTTF})_2\text{X}$ family. The ambient pressure positions of the charge-transfer salts with centrosymmetric anions $\text{X} = \text{SbF}_6, \text{PF}_6,$ and Br are indicated by arrows. 1D metal denotes the quasi-one-dimensional metallic properties, CO the charge-ordered phase, AFM stands for antiferromagnetism and SP for spin-Peierls state.

Under ambient conditions, these salts possess a quasi-one-dimensional metallic state, where the large anisotropy of their electronic properties is based in their stacked molecular structure. With decreasing temperature, the localization of charges takes place over a broad temperature range—a crossover rather than a phase transition. Salts with larger anions, like $X = \text{SbF}_6$ and TaF_6 , exhibit a charge-ordering phase transition at T_{CO} below the localization temperature T_ρ . At much lower temperatures $T_{\text{N}} < 10$ K, these compounds undergo a transition to an antiferromagnetic ground state. For salts with smaller anions, e.g., $X = \text{PF}_6$ and AsF_6 , a weaker charge order is observed at temperatures between 100 and 50 K [4]. In addition, these compounds exhibit a spin-Peierls ground state below 20 K. For compounds with even smaller anions, such as $X = \text{Br}$, no clear charge ordering can be observed; albeit there are indications that weak charge disproportionation takes place around 50 K [5,6]. Here again, antiferromagnetic ordering occurs at low temperatures. Salts containing tetrahedral anions, such as ClO_4 , ReO_4 and BF_4 , also exhibit some ordering of the anions; for that reason, they are not included in Figure 1. This structural phase transition normally occurs at temperatures T_{AO} well below the charge-ordering temperature [7–9]. In $(\text{TMTTF})_2\text{ClO}_4$, however, no charge ordering is observed at all; but the anion transition T_{AO} occurs below T_ρ .

As indicated in the phase diagram (Figure 1), the transitions (going from left to right) can be induced by increasing the external pressure by a few GPa. A similar effect can be seen when ‘internal pressure’ is increased, i.e., by reducing the anion size. Why this is so can be better understood when considering the molecular structure of these salts depicted in Figure 2: The anions, which are segregated between the TMTTF stacks, are positioned in a cage formed by the methyl groups terminating the TMTTF molecules. In a first approximation, the size of the anions determines the separation of the molecular stacks. The degree of this anion confinement in the methyl end-group cage also affects the anion ordering in the tetrahedral anion salts. Even more important, the anion-stack interaction enhances the dimerization within the TMTTF stacks and consequently suppresses charge order [10]. In other words, how freely the anion can move within the confined space affects the anisotropic charge transport in the salt as well as how charges localize and order with decreasing temperature down to their antiferromagnetic and spin Peierls ground states [11].

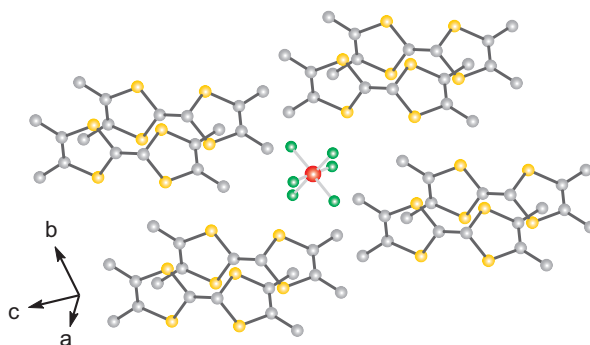


Figure 2. Molecular structure model of the $(\text{TMTTF})_2X$ salt. As a representative example, an octahedral salt, e.g., $(\text{TMTTF})_2\text{PF}_6$, is depicted here. All Fabre salts, containing octahedral, tetrahedral, or mono-atomic anions, have this triclinic crystal structure. The crystal structure is the same for undeuterated and deuterated samples investigated in this study.

In order to study these interactions—and more specifically, the effect of confinement of the anion within its methyl end-group cage—we compare protonated with deuterated Fabre salts: $(\text{TMTTF})_2X$, for anions $X = \text{Br}$, PF_6 , SbF_6 , and ClO_4 . When the hydrogen atoms in the CH_3 group are exchanged with the heavier deuterium isotope, the dynamics and interaction between the anion and its molecular neighbors are modified. A close comparison of the dc transport results obtained for deuterated and protonated samples should, therefore, provide valuable information on the electronic properties and elucidate further details of this intricate interplay.

In the present paper—after providing details of the experiments in Section 2—we present and discuss the results in Section 3. In the subsequent Section 4, the data are analyzed further with respect to various charge transport mechanisms.

2. Experimental Details

Single crystals of deuterated and protonated $(\text{TMTTF})_2\text{X}$ with $\text{X} = \text{Br}, \text{PF}_6, \text{SbF}_6, \text{ClO}_4$ were grown electrochemically in an H-type glass cell under ambient conditions, as described in Reference [7]. Needle shaped crystals, $\sim 1\text{--}2$ mm long, ~ 100 μm wide, and less than 100 μm thick, were harvested after several weeks. Here, we denote the hydrogenated $(\text{H}_{12}\text{C}_{10}\text{S}_4)_2\text{X}$ as $(\text{H}_{12}\text{-TMTTF})_2\text{X}$ and the deuterated analogue $(\text{D}_{12}\text{C}_{10}\text{S}_4)_2\text{X}$ is labelled $(\text{D}_{12}\text{-TMTTF})_2\text{X}$.

Direct current (dc) resistivity measurements were performed across a temperature range between 300 K and 4 K, at a ramp rate of $|0.3 \text{ K/min}|$ in a glass cryostat using liquid nitrogen and helium for cooling, while the sample chamber was flooded with helium gas to ensure thermal contact between the sample and the cryogenic chambers. The dc resistivity was measured along the molecular stacking direction, i.e., the long needle axis, referred to as the a -axis of the crystal (see Figure 2). In order to perform four-point measurements, four gold wires were attached to the crystal needle with carbon paste. Samples were anchored on a sapphire plate to ensure good thermal contact and electrical insulation from the cryostat's sample chamber. Data were collected while cooling down as well as while warming up. A Keithley 2612B system source meter and a Keithley 2182 nanovoltmeter were used to perform resistivity measurements. In order to protect the sample from overheating, the current was set to a constant value; the voltage was ramped across four linearly spaced points around 0 V to check the samples' Ohmic behavior when recording data at a certain temperature.

While the anisotropy of the Fabre salts is interesting by itself, and was elaborated upon in the previous study by Köhler et al. [7], here we focus on measurements along the a -axis, where the data quality is superior and most of the relevant information can be extracted.

3. Results and Discussion

The recorded dc resistivity versus temperature, $\rho(T)$ is plotted in Figure 3 for $(\text{TMTTF})_2\text{X}$, with the anions $\text{X} = \text{Br}, \text{PF}_6, \text{SbF}_6, \text{ClO}_4$, where in each of the panels, the respective protonated (black open squares) and deuterated (red solid diamonds) crystals are compared. All show an overall increase in resistivity upon cooling. The behavior can be typically traced up to the order of $10^6 \Omega\text{cm}$; beyond that bound, sample heating and non-Ohmic properties prevent reliable data acquisition. In the case of the rather good conductor $(\text{TMTTF})_2\text{Br}$, data are recorded down to $T = 4$ K. For the salts with larger anions, the resistivity measurements become non-Ohmic already below 20 K or even higher temperatures. The resistivity curve of $(\text{TMTTF})_2\text{Br}$ lies below its deuterated analogue, while for the other salts, the opposite behavior is observed. Arrows mark the charge order (CO) transition for the $(\text{TMTTF})_2\text{Br}$, $(\text{TMTTF})_2\text{PF}_6$ and $(\text{TMTTF})_2\text{SbF}_6$ salts, and the anion order (AO) transition in the $(\text{TMTTF})_2\text{ClO}_4$ samples (grey arrows for protonated, orange for deuterated crystals).

Table 1 summarizes all phase transition temperatures for the compounds under study. Upon being cooled down from room temperature, the samples exhibit metallic behavior, i.e., the resistivity decreases slightly with lowering temperature. Charges gradually localize and the metallic conductivity freezes: T_ρ is the localization temperature which occurs as a broad global minimum in the temperature dependent resistivity curves (Figure 3) and is defined as the temperature where the energy gap $\Delta(T) = 0$ in Figure 8 below. The change in localization temperature upon deuteration (see Table 2), i.e., $\Delta T_\rho = T_\rho^{\text{H}} - T_\rho^{\text{D}}$, ranges from tens to slightly more than one-hundred Kelvin. T_ρ increases upon deuteration for the Br, PF_6 , and SbF_6 salts, but decreases in $(\text{TMTTF})_2\text{ClO}_4$. Because this localization minimum is so shallow and broad, the uncertainties are rather large, as is reflected in the substantially differing T_ρ values reported in literature [7,12].

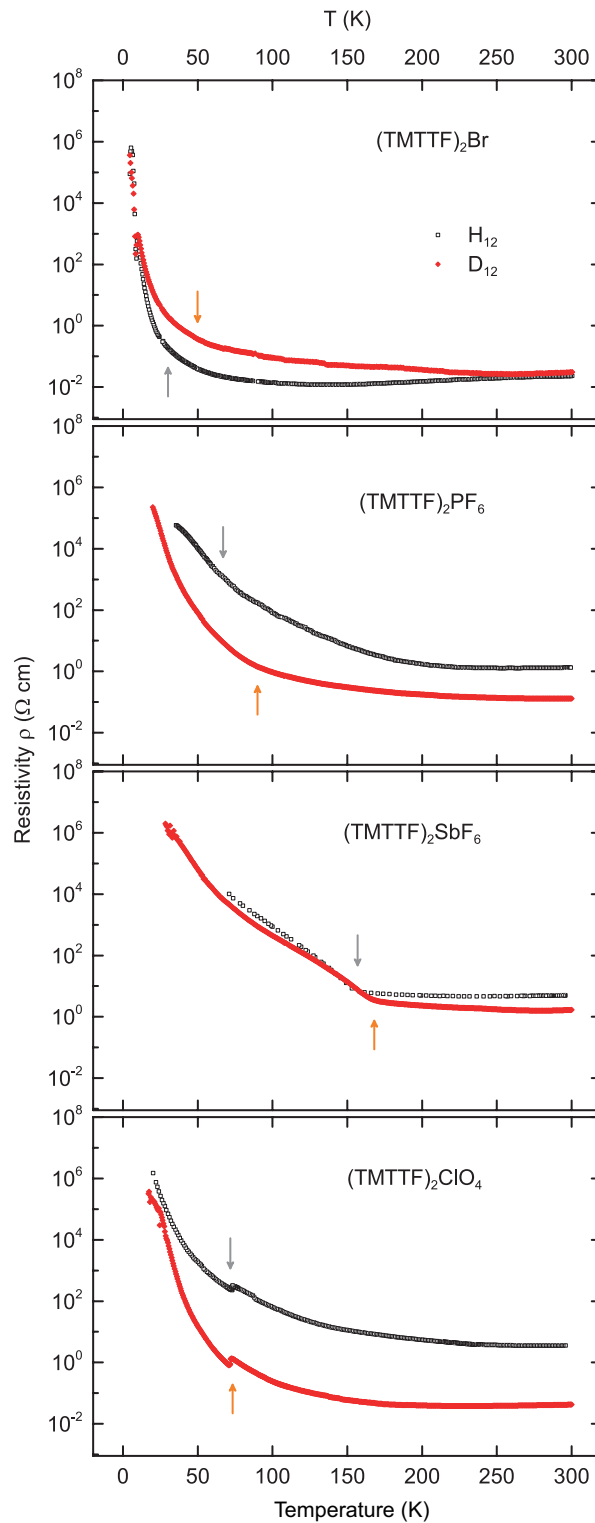


Figure 3. Temperature dependent dc resistivity $\rho(T)$ measured along the a -axis of deuterated (D_{12}) (red solid diamonds) and protonated (H_{12}) (black open squares) $(\text{TMTTF})_2\text{X}$ salts ($\text{X} = \text{Br}, \text{PF}_6, \text{SbF}_6, \text{ClO}_4$). Note the logarithmic vertical axes. Arrows mark the charge ordering [for $(\text{TMTTF})_2\text{Br}$, $(\text{TMTTF})_2\text{PF}_6$, $(\text{TMTTF})_2\text{SbF}_6$] and anion ordering [for $(\text{TMTTF})_2\text{ClO}_4$] transitions for the deuterated (orange) and protonated (grey) samples.

Table 1. Phase transition temperatures T_ρ , T_{CO} , T_{AO} , T_{SP} , T_N , for H_{12} - and $(D_{12}\text{-TMTTF})_2X$, with $X = \text{Br}$, PF_6 , SbF_6 , ClO_4 , as determined from the dc resistivity data plotted in Figure 3. Note that some temperatures are better identified in the alternative presentation displayed in Figure 8. Since the low-temperature magnetic phase transitions for the Br , PF_6 , and SbF_6 salts could not be resolved in our measurements, literature values are supplied for T_{SP} of H_{12} - and $(D_{12}\text{-TMTTF})_2\text{PF}_6$ compounds from References [7,13], as well as for T_N of the $(\text{TMTTF})_2\text{Br}$ and $(\text{TMTTF})_2\text{SbF}_6$ salts as they appear in the last column, from References [11,13–18].

Anions		Transition Temperatures (K)				
X		T_ρ	T_{CO}	T_{AO}	T_{SP}	T_N
Br	H_{12}	130	30			13
	D_{12}	260	50			19
PF_6	H_{12}	260	67		19	
	D_{12}	280	90		13	
SbF_6	H_{12}	240	157			6
	D_{12}	280	168			8
ClO_4	H_{12}	290		73.1		
	D_{12}	230		71.9		

Table 2. Changes observed in transition temperatures, ΔT , upon deuteration of the $(\text{TMTTF})_2X$ salts, calculated from values given in Table 1 using $\Delta T = T_*^H - T_*^D$ for the respective quantities. In the case of resistivity minimum T_ρ , the error bar may reach ± 25 K.

Anions		Change in Transition Temperature (K)				
X		ΔT_ρ	ΔT_{CO}	ΔT_{AO}	ΔT_{SP}	ΔT_N
Br		−130	−20			−6
PF_6		−20	−23		6	
SbF_6		−40	−11			−2
ClO_4		60		1.2		

For most Fabre salts, a transition to a $4k_F$ charge ordered state occurs at T_{CO} . In our compounds containing centrosymmetric anions, this transition is visible as a steepening in the slope of the resistivity curve observed upon cooling, and is especially strong in $(\text{TMTTF})_2\text{SbF}_6$, while being less pronounced in $(\text{TMTTF})_2\text{PF}_6$ and $(\text{TMTTF})_2\text{Br}$, see Figure 3. This observation is in agreement with the results previously reported [7]. For $(\text{TMTTF})_2\text{PF}_6$ and $(\text{TMTTF})_2\text{Br}$ the transitions in deuterated and protonated crystals are difficult to infer from the raw data $\rho(T)$, but can be identified in the temperature dependent energy gap plotted in Figure 8. The CO transition temperatures, as marked in our data, are listed in Table 1 [6,7,12–14]. T_{CO} increases upon deuteration, as seen in Table 2. The enhancement of the CO transition temperature is largest for small anions [10]. This can be explained in terms of the competition between CO and intrastack dimerization: with the latter decreasing upon deuteration, the CO transition shifts to higher T_{CO} [15].

Non-centrosymmetric anions can arrange in a regular alternation pattern; in the case of $(\text{TMTTF})_2\text{ClO}_4$ a clear anion ordering is observed at $T_{AO} = 73$ K. During this transition, a $2k_F$ superstructure forms along the stacking direction [12], which results from the orientation ordering of the tetrahedral anions in their TMTTF methyl cavity. Just to be clear, the anion order is mediated via the TMTTF stacks and not a direct interaction. For that reason, the coupling via the methyl groups is crucial. A zoomed-in view of the resistivity curves around this transition is presented in Figure 4. Here the cooling (solid symbols) and heating (open symbols) curves of the protonated (black symbols, top curve) and deuterated (red symbols, bottom curve) salts are plotted on a logarithmic resistivity and linear temperature axis. The hysteresis of this transition is more pronounced in the protonated sample ($T_{AO,H}^{\text{warming}} - T_{AO,H}^{\text{cooling}} = 1$ K) than in the deuterated sample ($T_{AO,D}^{\text{warming}} - T_{AO,D}^{\text{cooling}} = 0.4$ K). The hysteresis is well known from salts with non-centrosymmetric anions [7–9] and is an indicator of the first order nature of the AO phase transition. The broader hysteresis implies a stronger interaction of the anions

with the caging methyl groups. In other words, if no hysteresis is present, there is basically no potential barrier preventing the phase transition. However, since the difference in hysteresis between the deuterated and protonated samples lies within the error margins of the experiment, it will not be further analysed here [19]. The other striking characteristic of the AO transition is the downward (upward) jump in resistivity upon cooling (heating). The tiny variation in T_{AO} brought about by deuteration ($\Delta T_{AO} = 1.2$ K)—as summarized in Table 2—is about the uncertainty of this measurement. This agrees with previous experiments that could not resolve any difference upon deuteration [10]. This observation indicates that the interaction between the anion and TMTTF stacks depends, to a lesser extent, on the hydrogen bonds of the methyl groups (indicated by the dotted lines and red left arrow in Figure 5), and must therefore depend more strongly on the Coulomb interaction between the anion ligands and the TMTTF molecules' sulphur atom (green downward arrow) [10,11].

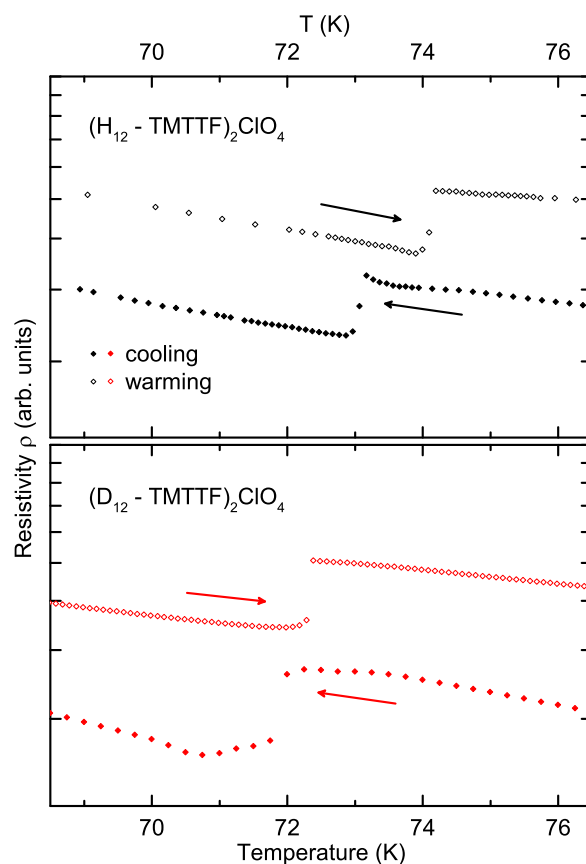


Figure 4. Anion transition of the protonated (black symbols, top panel) and deuterated (red symbols, bottom panel) $(\text{TMTTF})_2\text{ClO}_4$ crystals. Cooling (solid symbols, indicated by left arrow) and warming (open symbols, indicated by right arrow) are plotted to show the hysteresis. Note the logarithmic resistivity axis and linear temperature axis.

The structural aspects of the charge and anion ordering transitions have been discussed in detail by Pouget [11,12,20]. Figure 5 illustrates the processes involved in stabilizing the states. Charge order in salts containing centrosymmetric anions (PF_6 , SbF_6 , and possibly Br) are most likely stabilized via the deformation of the methyl end group cavity—the process marked by the red left arrow. In this process, the displacement of the anion, X, polarizes the hydrogen bond network inside the cavity. This, in turn, causes a displacement of the charge on the σ -bonds connected to the hydrogen bonds, shifting the σ -electrons towards the center of the TMTTF molecules, which stabilizes the excess π -holes on the molecules (indicated by the grey ovals in Figure 5). This hypothesis is sustained by the fact that T_{CO} rises with larger anion size and upon deuteration—in both cases, the contact between the anion and its cavity periphery, i.e., the methyl end groups, increases. The second process proposed in reference [11],

indicated by the green downward arrow in Figure 5, is that the anion moves towards the sulphur atom of the TMTTF molecule. This directly shortens the anion–sulphur contact distance and would also stabilize the enhanced π -hole density of the TMTTF molecule towards which the anion moves (different π -hole distribution than for the first process; not indicated in Figure 5). This second process is not substantiated experimentally for the charge-order transition, since structural refinement provides no evidence of a sizeable change in the anion-sulphur distance below T_{CO} for the centrosymmetric anion salts [11]. For the anion ordering transition, however, this second process seems to be a likely driving force in most tetrahedral anion salts, even though only very weak changes in the anion-sulphur distance have been reported below T_{AO} for $(TMTTF)_2ClO_4$ [11].

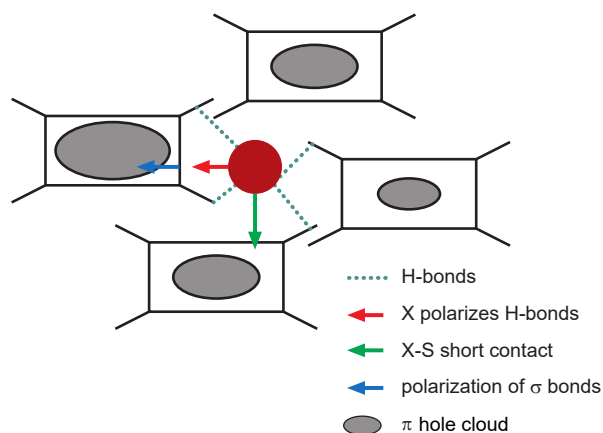


Figure 5. A schematic representation of the molecular structure of $(TMTTF)_2X$ salts. The rectangles represent the TMTTF molecules with their methyl end groups (four ‘legs’ sticking out). The latter form a cage between the organic molecules containing the anion, X (filled dark red sphere in the diagram). Depending on the size of the anion and the methyl end-groups (whether they are deuterated or protonated) this cage forms a spacious or a more confined trap for the anion to move about in. The blue dotted lines represent the hydrogen bonds forming between the anion and the methyl end groups. Figure adapted from Pouget [11].

Tables 1 and 2 list the transition temperatures and the difference resulting from deuteration for the spin-Peierls transitions T_{SP} in $(TMTTF)_2PF_6$ and the antiferromagnetic transitions T_N in $(TMTTF)_2SbF_6$ and $(TMTTF)_2Br$ samples as well, obtained by magnetic probes [18,21]. From our transport experiments on both protonated and deuterated $(TMTTF)_2Br$ down to $T = 4$ K, we can access the antiferromagnetic transitions located at $T_N = 13$ K and 19 K, respectively [11,14]. Figure 6 zooms into this low-temperature region of the warming (open symbols) and cooling (solid symbols) $\rho(T)$ curves of the protonated (black symbols, top panel) and deuterated (red symbols, bottom panel) Br-salts. T_N , as reported in Table 1, is marked by the grey (orange) arrow for the protonated (deuterated) crystal. The antiferromagnetic transition cannot be distinguished for the $(H_{12}-TMTTF)_2Br$ compound, while there seems to be a slight bump in the warming curve of $(D_{12}-TMTTF)_2Br$ at 19 K. This, however, does not exceed the experimental uncertainty sufficiently and should therefore not be interpreted as strong indication of the antiferromagnetic transition. Temperature dependent resistivity measurements performed by Tomić et al. have revealed anomalies at $T = 12.5$ K and 22 K in protonated $(TMTTF)_2Br$ [22]. Our cooling curves in Figure 6 show no clear evidence of an anomaly around 22 K. However, between 10 K and 7 K, the cooling curves of both crystals exhibit a pronounced dip with a minimum at 9 K (8 K) for the protonated (deuterated) salt. The underlying cause for this pronounced anomaly is as yet unclear.

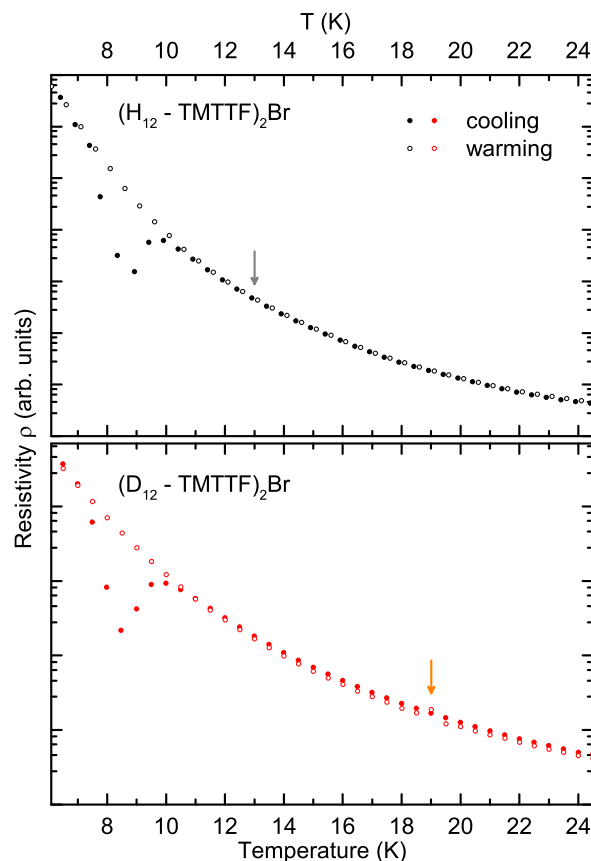


Figure 6. Resistivity $\rho(T)$ in the low-temperature regime of the protonated (black symbols, top panel) and deuterated (red symbols, bottom panel) of the $(\text{TMTTF})_2\text{Br}$ compounds: cooling (solid symbols) and warming (open symbols). Arrows indicate the AFM transition temperatures obtained by magnetic probes.

4. Analysis of the Transport Mechanisms

In the following, we analyze and discuss the charge-transport mechanisms and the temperature dependent energy gap, respectively.

4.1. Charge Transport Mechanisms

There are a variety of models to describe the charge transport in organic compounds, ranging from the classical band transport to various hopping transport mechanisms. The underlying mechanism of band transport involves a delocalized molecular wavefunction over the entire volume of the crystalline sample with mean free paths larger than the inter-site distance—usually occurring in highly ordered systems. Hopping transport, on the other hand, is described by transitions between localized sites via tunneling or overcoming potential barriers, the mean free path being on the order of the inter-site distance, and mostly governs electronic properties in more disordered systems. Since the appropriate models depend on the concentration of localized states, carrier density, and electric field strength (among other factors), charge transport within the same sample may have to be described using different models, depending on the temperature range and applied field.

Band transport is applicable for high carrier densities and described by the Arrhenius model, based on an activated temperature dependence of the charge carrier concentration. A linear slope on a graph of logarithmic resistivity versus inverse temperature (left column in Figure 7) indicates band transport in the respective temperature range. Explicitly, the Arrhenius law is given by

$$\rho(T) = \rho_0 \exp\left\{\frac{\Delta}{T}\right\}, \quad (1)$$

where the energy gap Δ is assumed to be temperature independent and ρ_0 is a constant prefactor [23]. This thermally activated transport was mostly observed along the c -axis of the crystal [7], i.e., perpendicular to the axis investigated here.

Variable range hopping is a phonon-activated process where charge carriers hop between localized states. This effect can be described in terms of a general formula proposed by Mott:

$$\rho(T) \propto \exp\left\{\left(\frac{T_0}{T}\right)^{1/\gamma}\right\}, \quad (2)$$

where $\gamma = d + 1$ is related to the dimension d of the system [24]. Mott variable-range hopping in three dimensions (right column in Figure 7) assumes a constant density of states. Efros and Shklovskii showed that, at sufficiently low temperatures, the density of states near the Fermi energy is not constant, but vanishes linearly [25–27], thus accounting for the so-called Coulomb gap, and resulting in a resistivity dependence of Equation (2) with $\gamma = 2$ (central column in Figure 7) in all dimensions—this transport regime being referred to as Efros–Shklovskii variable-range hopping [7,28,29]. For some samples, the disorder may be so high that the Coulomb gap is dominant at all temperatures, leading to overall Efros–Shklovskii hopping. In samples displaying relatively low disorder, on the other hand, the energy scale is such that the carriers may have enough energy to overcome the Coulomb gap at all measurable temperatures, meaning that the density of states is practically constant, leading to overall Mott variable-range hopping [25]. At intermediate disorder, it may be possible to see a crossover from Mott to Efros–Shklovskii hopping with decreasing temperatures in the same samples [30]. Köhler et al. found three-dimensional Mott hopping transport to dominate below 60 K along the stacking axis [7], i.e., the orientation investigated in the present study.

For data analysis, the resistivity was plotted on a logarithmic y -axis versus the inverse temperature, i.e., T^{-1} , as well as $T^{-1/2}$, and $T^{-1/4}$, in Figure 7. A linear slope in the Arrhenius plot would mean that band transport is valid across the applicable temperature range. Similarly, a linear slope in the $\ln\{\rho\}$ versus $T^{-1/2}$ plot indicates Efros–Shklovskii variable-range hopping, while a linear slope in the $\ln\{\rho\}$ versus $T^{-1/4}$ plot is an indication of three-dimensional hopping. Figure 7 compares all three transport models (from left to right) for all four Fabre salts under study (from top to bottom) with protonated and deuterated molecules (open black and solid red symbols, respectively). The arrows indicate the transition temperatures: the localization temperature T_ρ being the left most arrows in each panel, and the ordering transitions T_{CO} or T_{AO} being the right arrows (all other transition temperatures were omitted for clarity). The bottom axes are linear in T^{-1} , $T^{-1/2}$, and $T^{-1/4}$, from left to right, while the top axes indicate the converted temperature in Kelvin. Linear fits to the slopes were performed for the temperature ranges 300 K to T_ρ , T_ρ to T_{CO} or T_{AO} , and temperatures below T_{CO} or T_{AO} . The results are summarized in Table A1 (see Appendix A).

The range above T_ρ shows metallic behavior, i.e., the resistivity decreases upon cooling, and none of the above models apply. Below the localization temperature, all samples show an upturn in resistivity, indicating semiconducting behavior, which can be described by activated band transport or variable-range hopping.

In the range between T_ρ and T_{AO} , the protonated (TMTTF)₂Br salt exhibits a slight kink around $T = 60$ K. Above and below this kink, straight lines could be fitted over similar temperature ranges for all three transport models; hence, no firm conclusion can be drawn from the data about the dominant transport mechanism in this sample. For the deuterated compound of the Br-salt, the Efros–Shklovskii variable-range hopping model could be fitted across the largest temperature range, 255 K–54 K. This may be taken as an indication that the system is rather disordered, as mentioned in the discussion above. The deuterated compound shows a kink around 25 K, in the range between T_{CO} and T_N , which is close to the 22 K anomaly reported by Tomić et al. [22].

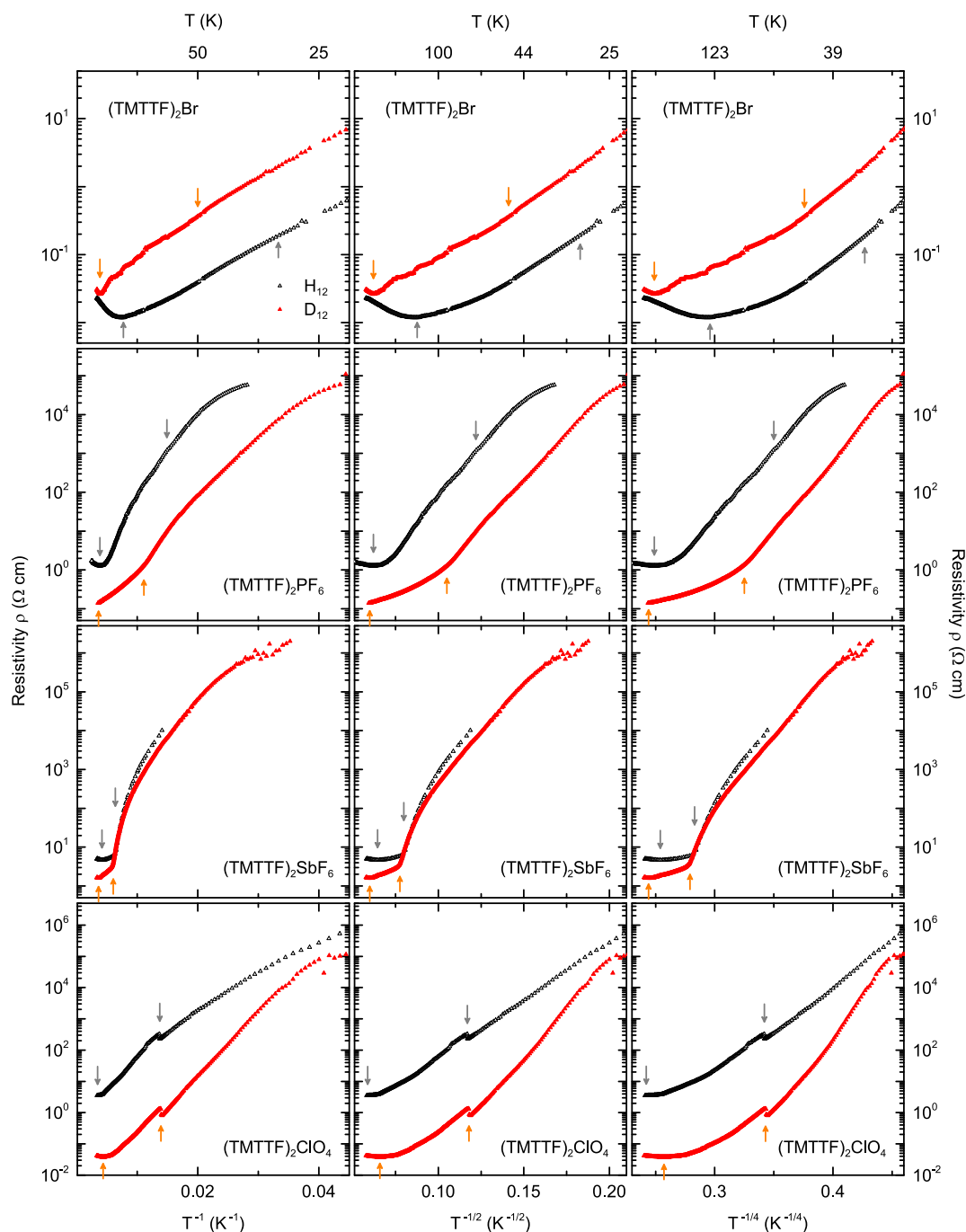


Figure 7. Comparison between three transport models, namely, Arrhenius (left column), three-dimensional variable-range hopping with Coulomb gap considered according to Efros and Shklovskii (central column) and three-dimensional Mott variable-range hopping without electronic correlations (right column), for all four protonated (shown by black symbols) and deuterated (red) salts (top to bottom). A given model is relevant in regions where the corresponding curves are linear. Supplementary data regarding the linear fits are provided in Table A1 (see Appendix A).

In (H₁₂-TMTTF)₂PF₆, the resistivity follows a behavior corresponding to three-dimensional Mott variable-range hopping that extends beyond the T_{ρ} - T_{CO} range to low temperatures. The deuterated counterpart has a kink around $T = 160$ K and exhibits variable-range hopping across an extended range below T_{CO} as well. This indicates that the (TMTTF)₂PF₆ salts are more ordered systems than the deuterated Br-salt.

The other salt containing an octahedral anion, $(\text{TMTTF})_2\text{SbF}_6$, exhibits three-dimensional variable-range hopping according to Mott from T_p to T_{CO} with a kink around $T = 190$ K in the protonated compound, extending to lower temperatures with another kink. The deuterated analogue, on the other hand, shows no clear match to any of the three models at higher temperatures. However, in the low-temperature range, it might exhibit some variable-range hopping.

$(\text{TMTTF})_2\text{ClO}_4$ does not undergo any pure CO transition, but a pronounced AO transition slightly above 70 K. No significant change in slope is expected across a simple structural transition at T_{AO} when the transport mechanism remains the same; this was observed in other Fabre salts with tetrahedral anions [7,8], for instance. In the Arrhenius plot (left column of Figure 7), we find the slope before and after the AO transition to be rather similar only for the deuterated compound. In other words, $(\text{D}_{12}\text{-TMTTF})_2\text{ClO}_4$ exhibits an activated behavior with the same energy gap Δ on both sides of the phase transition, as analyzed in Table A1 (see Appendix A). For the protonated sister compound, however, the slope in the Arrhenius plot differs before and after the AO transition. The hopping model in the central column of Figure 7, however, may indicate that the sample is so disordered that Efros–Shklovskii variable-range hopping is present across the entire temperature range.

To summarize our findings on the discussed transport mechanisms at play in the deuterated and protonated Fabre salts investigated—between room temperature and their localization crossover temperature, T_p —all compounds display metallic behavior. Below this, all samples show semiconducting behavior, which can be described best by an activated band transport model, or variable-range hopping. The resistivity of $(\text{D}_{12}\text{-TMTTF})_2\text{Br}$ follows Efros–Shklovskii model across a broad temperature range, indicating it to be a more disordered system than the other compounds. $(\text{H}_{12}\text{-TMTTF})_2\text{SbF}_6$ and both types of $(\text{TMTTF})_2\text{PF}_6$ could be fitted with Mott variable-range hopping over a broad temperature range extending below their respective charge-order transition temperatures—an indication for ordered systems. This finding agrees with previous studies [7], where variable-range hopping transport was found to dominate below $T = 60$ K in octahedral $(\text{TMTTF})_2\text{X}$ salts. $(\text{D}_{12}\text{-TMTTF})_2\text{ClO}_4$ could be fitted by an Arrhenius model with the same slope above and below its anion transition, indicating band transport with a constant activation energy across the phase transition, while the behavior observed in the protonated sister compound is best fitted by Efros–Shklovskii variable-range hopping across the AO phase transition, indicating a temperature dependent energy gap in this system.

4.2. Energy Gap

The above discussion illustrates that band transport is not necessarily the best overall model applicable to these samples; certainly, the electrical resistivity $\rho(T)$ cannot be simply described by a temperature independent energy gap, like in Equation (1). In particular, when considering the charge ordering as a second-order phase transition, the energy gap should follow a mean-field temperature dependence [7]. In order to investigate this further, the temperature dependent gap

$$\Delta(T) = \ln \left\{ \frac{\rho(T)}{\rho_0} \right\} T, \quad (3)$$

was deduced from Equation (1) and plotted in Figure 8 for all samples under investigation. Equation (3) assumes constant ρ_0 , the values of which are listed in Table 3.

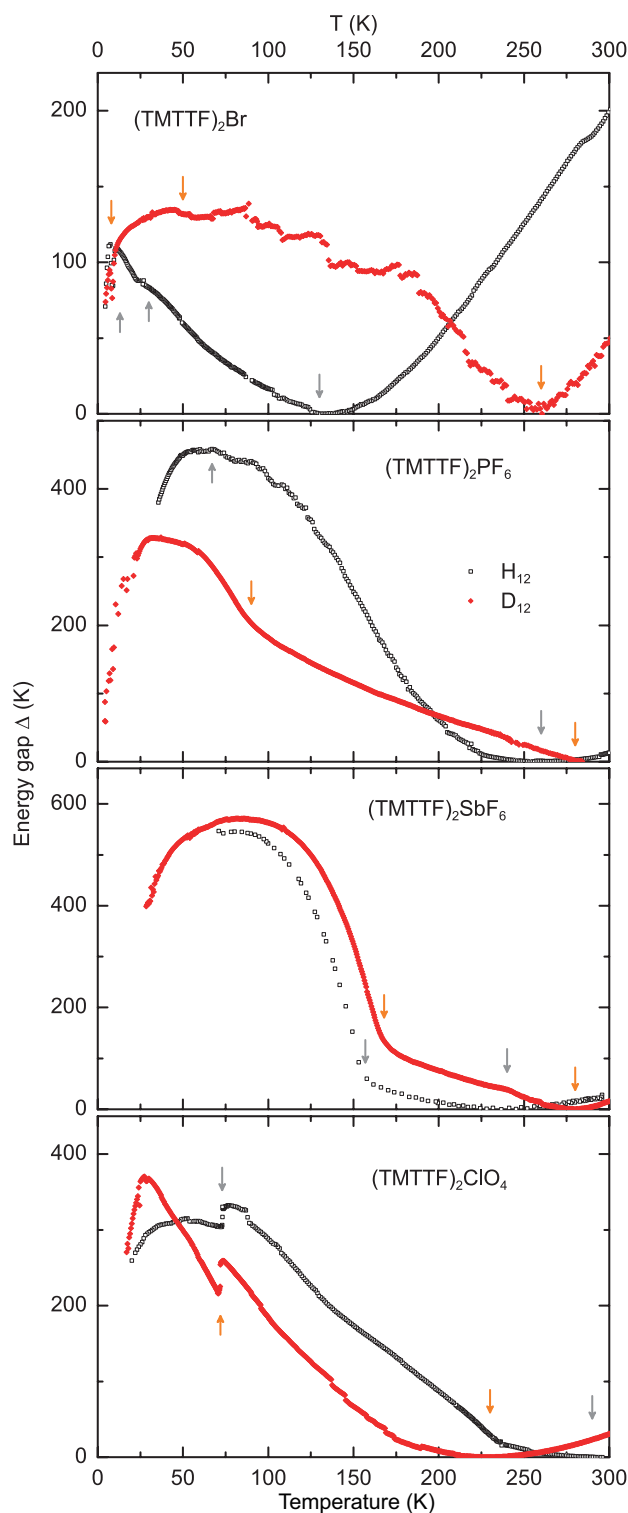


Figure 8. Temperature dependent energy gap $\Delta(T)$ for the protonated (black symbols) and deuterated (red dots) Fabre salts $(\text{TMTTF})_2X$ ($X = \text{Br}, \text{PF}_6, \text{SbF}_6$ and ClO_4) as calculated via Equation (3). The right most orange (grey) arrows indicate T_ρ of the deuterated (protonated) compounds. From right to left, the next set of arrows indicate the charge and anion ordering transitions T_{CO} or T_{AO} , while the left most set of arrows in the top panel [$(\text{TMTTF})_2\text{Br}$ salts] indicate the AFM ordering at T_{N} .

Table 3. The constant resistivity ρ_0 from Equation (3) for the protonated and deuterated Fabre salts (TMTTF)₂Br, (TMTTF)₂PF₆, (TMTTF)₂SbF₆ and (TMTTF)₂ClO₄, as determined for Figure 8. The energy gap at the localization temperature T_ρ was set to zero by adjusting ρ_0 .

Anions X		ρ_0 (Ωcm)
Br	H ₁₂	0.01184
	D ₁₂	0.02606
PF ₆	H ₁₂	1.286
	D ₁₂	0.1401
SbF ₆	H ₁₂	4.638
	D ₁₂	1.585
ClO ₄	H ₁₂	3.557
	D ₁₂	0.03818

The presentation of the temperature dependent energy gap in Figure 8 makes all discussed phase transitions at T_ρ , T_{CO} , and T_{AO} clearly visible; one has to keep in mind, however, that the values in the metallic regime are not physically meaningful. Below T_ρ different regions of varying gap-behavior can be distinguished. For (TMTTF)₂Br the energy gap Δ_0 is attributed to the bond dimerization resulting in unequal charge distribution between molecules [7]. Further cooling through T_{CO} causes stronger charge disproportionation between the molecules. Because of the second-order nature of this transition, the corresponding energy gap shows a BCS-like increase. The AO transition occurring in tetrahedral samples at lower temperatures was also found to contribute in a mean-field fashion. The total energy gap is given by [7]

$$\Delta(T) = \sqrt{\Delta_0^2 + [\Delta_{\text{CO}}(T) + \Delta_{\text{AO}}(T)]^2} \quad (4)$$

The gaps extracted from Figure 8 are summarized in Table 4, where further details are given. The localization energy gap, Δ_0 , is highest in the (TMTTF)₂PF₆ and (TMTTF)₂ClO₄ compounds, where deuteration reduces the value. The opposite is true for (TMTTF)₂Br and (TMTTF)₂SbF₆ salts, which show similar values for this gap. The charge-order gap, Δ_{CO} , exhibits a clear trend, increasing with anion size from just above 100 K for the protonated Br-salt to almost 600 K in the deuterated SbF₆-compound. The anion gap, Δ_{AO} , for (TMTTF)₂ClO₄ was read off directly from the plot. Since these compounds show no CO transition and the AO causes only little change of slope in the Arrhenius plot, Δ_{AO} can be set to zero for this special case [7]. The abrupt changes in resistivity are attributed to the prefactor ρ_0 in Equation (1). The fact that the value of Δ_{AO} is smaller than Δ_0 for (TMTTF)₂ClO₄ seems to be unphysical. For the deuterated sample, however, a simple Arrhenius fit could be identified rather well (Figure 7), and correspondingly no discrepancies were found in the activation energy values. Hence, the ClO₄-salts seem to pose a challenge to the analysis proposed so far and further investigation is necessary to clarify this case. The total energy gap—last column in Table 4—also reveals a trend of increasing gap energy with increasing anion size. For all samples, except the (TMTTF)₂PF₆ salts, the deuterated compounds exhibit higher total gap energies than their protonated counterparts.

The increase in charge order gap energy and total gap energy with increasing anion size and upon deuteration (in general), indicates that the deformation of the methyl end-group cavity has a significant effect on the charge order transition—and thus confirms the deuteration and anion size effect shown in the trend of the change in T_{CO} . In a next step, local probes should be applied to monitor the charge distribution in these compounds, and in particular, how it varies with temperature and deuteration.

Table 4. Energy gaps for $(\text{TMTTF})_2X$ ($X = \text{Br}, \text{PF}_6, \text{SbF}_6$ and ClO_4) as read off Figure 8. As suggested by Köhler et al., Δ_0 was extracted at T_{CO} , while Δ_{CO} and Δ_{AO} were read off at the highest point between T_{CO} or T_{AO} and $T \rightarrow 0$ K, respectively. Δ is the total gap energy as calculated according to Equation (4).

Anions X		Δ_0 (K)	Δ_{CO} (K)	Δ_{AO} (K)	Δ (K)
Br	H ₁₂	90	110		140
	D ₁₂	130	135		190
PF ₆	H ₁₂	460	460		650
	D ₁₂	200	330		390
SbF ₆	H ₁₂	60	545		550
	D ₁₂	140	570		585
ClO ₄	H ₁₂	330		315	450
	D ₁₂	260		370	450

5. Summary

This comparative study between deuterated and protonated Fabre salts aimed to advance our understanding how the methyl end-groups effect the electronic properties in quasi-one-dimensional charge transfer salts. The different anions are dynamically confined by the terminal methyl groups and their interaction affects the electronic properties and phase transitions. The dc resistivity measurements performed along the stacking axis of the centrosymmetric and tetrahedral $(\text{TMTTF})_2X$ salts and the data analysis, considering different transport models and a temperature dependent energy gap, have ascertained that the charge ordering transition is strongly affected by the methyl end-group cavity in which the anions are trapped: The change in T_ρ and T_{CO} , as well as the energy gap, increase upon deuteration and with increasing anion size. For the centrosymmetric anion salts, variable range hopping was confirmed to describe the charge transport in these samples best. $(\text{TMTTF})_2\text{ClO}_4$ showed band transport behavior across its anion ordering phase transition. Overall, deuteration seems to have a similar effect on the system as an increase in anion size.

Author Contributions: Conceptualization and supervision, M.D.; synthesis of deuterated molecules, T.N.; investigation and analysis, A.R.; writing and editing, A.R. and M.D. All authors have read and agreed to the published version of the manuscript.

Funding: The project was supported by the Deutsche Forschungsgemeinschaft (DFG).

Acknowledgments: We acknowledge continuous crystal growth and thorough sample preparation by G. Untereiner; deuterated TMTTF crystals were grown by A. Moradpour. We acknowledge fruitful discussions with E. Rose and finally thank R. Rösslhuber and D. Liu for experimental support.

Conflicts of Interest: The authors declare no conflict of interest.

Appendix A

Table A1. Summary of linear fit parameters of the plots $\rho(T)$ vs. T^{-1} , $T^{-1/2}$, and $T^{-1/4}$ in Figure 7.

		#Linear Fit# over Entire# Temp Range	Best# Linear# Fit	Linear Fit# over Entire# Temp Range	Best# Linear# Fit			Linear Fit# over Entire# Temp Range	Best# Linear# Fit		
(TMTTF) ₂ X		300 K- T_p			$T_p T_{CO}$ or T_{AO}			T_{AO} or $T_{CO}T_N$ or T_{SP} or 4 K			
actual temperature range (K)		300–130			130–30			30–13			
H ₁₂ -Br	T^{-1}	best fit temp range (K)	300–180		130–60	60–30			24–13		
		slope	−89.595	−106.554	48.078	38.048	52.804	54.757	57.149		
		y-intercept	−1.352	−1.282	−2.349	−2.233	−2.457	−2.598	−2.741		
	$T^{-1/2}$	best fit temp range (K)	300–181		130–61	60–27			24–13		
		slope	−11.206	−14.082	12.462	8.118	16.354	24.579	26.979		
		y-intercept	−1.005	−0.819	−3.126	−2.662	−3.711	−5.317	−5.899		
$T^{-1/4}$	best fit temp range (K)	300–167		130–63	49–27			22–10			
	slope	−6.044	−7.076	8.819	5.167	13.597	25.026	29.727			
	y-intercept	−0.193	0.069	−4.671	−3.482	−6.529	−11.669	−13.983			
actual temperature range (K)		300–260			260–50			50–8			
D ₁₂ -Br	T^{-1}	best fit temp range (K)	295–260		157–174	173–89	89–48		50–25	25–10	
		slope	−127.055	−119.421	71.181	141.631	74.232	54.111	40.052	52.862	42.037
		y-intercept	−1.096	−1.124	−1.789	−2.146	−1.789	−1.537	−1.050	−1.461	−1.002
	$T^{-1/2}$	best fit temp range (K)	295–260		255–54				50–25	25–10	
		slope	−15.423	−14.362	14.053	13.994		18.514	17.777	21.234	
		y-intercept	−0.628	−0.692	−2.443	−2.438		−3.047	−2.942	−3.640	
$T^{-1/4}$	best fit temp range (K)	295–261		257–177	186–67	67–48		50–25	25–10		
	slope	−7.535	−6.995	8.638	10.224	8.547	11.621	17.357	14.510	21.126	
	y-intercept	0.292	0.159	−3.751	−4.155	−3.730	−4.816	−7.047	−5.896	−8.875	
actual temperature range (K)		300–260			260–67			67–19 (data ends at 35)			
H ₁₂ -PF ₆	T^{-1}	best fit temp range (K)	300–260		200–107	109–67		100–51			
		slope	−34.808	(not linear)	299.215	371.644	235.220	132.518	211.301		
		y-intercept	0.240		−1.166	−1.650	−0.419	1.274	−0.124		
	$T^{-1/2}$	best fit temp range (K)	300–260		181–65				124–47		
		slope	−4.125	(not linear)	53.106	56.448		38.392	50.922		
		y-intercept	0.363		−3.432	−3.758		−1.483	−3.168		
$T^{-1/4}$	best fit temp range (K)	300–260		188–44				67–35			
	slope	−1.974	(not linear)	31.610	34.964		29.290	(see previous range)			
	y-intercept	0.598		−8.103	−9.142		−7.059	(see previous range)			
actual temperature range (K)		300–280			280–90			90–13 (good data up to 20)			
D ₁₂ -PF ₆	T^{-1}	best fit temp range (K)	300–280		239–119	157–90		59–30			
		slope	4.722	(too small)	124.022	115.341	139.517	148.637	151.236		
		y-intercept	−0.869		−1.325	−1.282	−1.458	−1.221	−1.113		
	$T^{-1/2}$	best fit temp range (K)	300–280		287–161	163–101			87–26		
		slope	0.532	(too small)	20.038	14.253	23.332	46.486	47.952		
		y-intercept	−0.883		−2.115	−1.710	−2.426	−4.693	−4.879		
$T^{-1/4}$	best fit temp range (K)	300–280		280–155	163–103			89–23			
	slope	0.268	(too small)	11.213	7.761	13.707	36.144	36.353			
	y-intercept	−0.917		−3.675	−2.764	−4.438	−11.642	−11.717			

Table A1. Cont.

		#Linear Fit# over Entire# Temp Range	Best# Linear# Fit	Linear Fit# over Entire# Temp Range	Best# Linear# Fit	Linear Fit# over Entire# Temp Range	Best# Linear# Fit	
	actual temperature range (K)	300–240			240–157		157–8 (good data ends at 70)	
H ₁₂ -SbF ₆	best fit temp range (K)		296–251		228–165 (not linear)		110–70 (not linear)	
	T^{-1} slope	–47.048	–54.097	70.625	66.416	393.592	273.853	
	T^{-1} y-intercept	0.859	0.884	0.351	0.367	–1.177	0.196	
	best fit temp range (K)		296–249		219–165 (not linear)		157–114 112–70	
	$T^{-1/2}$ slope	–5.746	–6.532	10.123	10.124	78.505	121.771 59.678	
	$T^{-1/2}$ y-intercept	1.034	1.081	–0.011	–0.018	–5.042	–8.825 –3.043	
H ₁₂ -SbF ₆	best fit temp range (K)		297–252		234–182 199–157		157–114 116–71	
	$T^{-1/4}$ slope	–2.734	–3.209	5.413	3.589 7.915	49.339	71.707 38.894	
	$T^{-1/4}$ y-intercept	1.359	1.475	–0.734	–0.256 –1.421	–12.770	–19.378 –9.373	
	actual temperature range (K)	300–280			280–166		166–8 (good data to 27)	
D ₁₂ -SbF ₆	best fit temp range (K)		300–286		231–181		111–64 (not linear)	
	T^{-1} slope	–101.615	–126.631	134.304	128.026	203.142	247.267	
	T^{-1} y-intercept	0.560	0.644	–0.296	–0.274	0.336	0.176	
	best fit temp range (K)		300–287		231–184		112–44	
	$T^{-1/2}$ slope	–11.269	–14.926	18.243	17.713	52.762	52.129	
	$T^{-1/2}$ y-intercept	0.871	1.084	–0.912	–0.886	–2.845	–2.557	
D ₁₂ -SbF ₆	best fit temp range (K)		300–286		229–183		126–38	
	$T^{-1/4}$ slope	–5.666	–7.150	9.511	9.482	37.198	36.190	
	$T^{-1/4}$ y-intercept	1.582	1.940	–2.150	–2.154	–9.280	–8.818	
	actual temperature range (K)	300–290			290–73		74–72 73–4 (good data ends at 20)	
H ₁₂ -ClO ₄	best fit temp range (K)		300–290		232–73.2 87–73.2		73.17–72.87 72.5–52 53–29	
	T^{-1} slope	4.567	(too small)	204.468	209.608	147.605	–2694.026 116.853	147.693 119.150
	T^{-1} y-intercept	0.536		–0.264	–0.316	0.495	39.318 0.838	0.334 0.903
	best fit temp range (K)		300–290		233–131 130–88 87–73.0		73.17–72.82 72.6–54 72–24	
	$T^{-1/2}$ slope	0.533	(too small)	35.389	28.927	43.917 31.979	–630.607 37.248	36.931 37.704
	$T^{-1/2}$ y-intercept	0.520		–1.723	–1.304	–2.591 –1.233	73.220 –2.002	–1.970 –2.063
H ₁₂ -ClO ₄	best fit temp range (K)		300–290		237–136 138–89 87–73.1 135–73.1		73.17–72.87 72.8–53 53–22 72.6–22	
	$T^{-1/4}$ slope	0.257	(too small)	21.392	15.578	26.857 22.312 27.831	–308.947 29.329	26.114 30.649 29.310
	$T^{-1/4}$ y-intercept	0.489		–4.929	–3.397	–6.691 –5.118 –6.988	108.098 –7.715	–6.583 –8.268 –7.709
	actual temperature range (K)	300–230			230–73		73–70 73–4 (good data to 18)	
D ₁₂ -ClO ₄	best fit temp range (K)		300–230		138–71.1 90–72.4		72.23–70.74 70.6–56 70.4–29	
	T^{-1} slope	–44.010	(not linear)	172.713	197.157	193.418	–655.223 167.089	220.575 208.745
	T^{-1} y-intercept	–1.234		–2.309	–2.569	–2.514	0.137 –2.198	–3.206 –3.014
	best fit temp range (K)		300–230		137–96 96–72.2		72.26–70.73 70.8–57 56–30	
	$T^{-1/2}$ slope	–5.544	(not linear)	30.793	33.654	43.408	–185.305 56.477	55.196 64.775
	$T^{-1/2}$ y-intercept	–1.060		–3.641	–3.989	–4.948	21.896 –6.765	–6.656 –7.990
D ₁₂ -ClO ₄	best fit temp range (K)		300–230		95–72.1 72.24–70.74		70.6–56 70.9–43 46–25	
	$T^{-1/4}$ slope	–2.778	(not linear)	18.215	20.594	28.769	–106.880 45.719	39.238 41.638 55.276
	$T^{-1/4}$ y-intercept	–0.712		–6.314	–7.137	–9.713	36.728 –15.919	–13.627 –14.473 –19.754

References and Notes

1. Lebed, A. (Ed.) *The Physics of Organic Superconductors and Conductors*; Springer: Berlin, Germany, 2008
2. Dressel, M. Spin-charge separation in quasi one-dimensional organic conductors. *Naturwissenschaften* **2003**, *90*, 337–344. [[CrossRef](#)] [[PubMed](#)]
3. Dressel, M. Ordering phenomena in quasi-one-dimensional organic conductors. *Naturwissenschaften* **2007**, *94*, 527–541. [[CrossRef](#)] [[PubMed](#)]
4. Dressel, M.; Dumm, M.; Knoblauch, T.; Masino, M. Comprehensive optical investigations of charge order in organic chain compounds (TMTTF)₂X. *Crystals* **2012**, *2*, 528–578. [[CrossRef](#)]
5. Nad, F.; Monceau, P.; Fabre, J.M. Low frequency dielectric permittivity of quasi-one-dimensional conductor (TMTTF)₂Br. *Eur. Phys. J. B* **1998**, *3*, 301–306. [[CrossRef](#)]
6. Coulon, C.; Lalet, G.; Pouget, J.P.; Foury-Leylekian, P.; Mouradpour, A.; Fabre, J.M. Anisotropic conductivity and charge ordering in (TMTTF)₂X salts probed by ESR. *Phys. Rev. B* **2007**, *76*, 085126. [[CrossRef](#)]
7. Köhler, B.; Rose, E.; Dumm, M.; Untereiner, G.; Dressel, M. Comprehensive transport study of anisotropy and ordering phenomena in quasi-one-dimensional (TMTTF)₂X salts (X = PF₆, AsF₆, SbF₆, BF₄, ClO₄, ReO₄). *Phys. Rev. B* **2011**, *84*, 035124. [[CrossRef](#)]
8. Rose, E.; Dressel, M. Coupling between molecular chains and anions in (TMTTF)₂X salts. *Phys. B Condens. Matter* **2012**, *407*, 1787–1792. [[CrossRef](#)]
9. Rösslhuber, R.; Rose, E.; Ivek, T.; Pustogow, A.; Breier, T.; Geiger, M.; Schrem, K.; Untereiner, G.; Dressel, M. Structural and Electronic Properties of (TMTTF)₂X Salts with Tetrahedral Anions. *Crystals* **2018**, *8*, 121. [[CrossRef](#)]
10. Pustogow, A.; Peterseim, T.; Kolatschek, S.; Engel, L.; Dressel, M. Electronic correlations versus lattice interactions: Interplay of charge and anion orders in (TMTTF)₂X. *Phys. Rev. B* **2016**, *94*, 195125. [[CrossRef](#)]
11. Pouget, J.P. Structural Aspects of the Bechgaard and Fabre Salts: An Update. *Crystals* **2012**, *2*, 466–520. [[CrossRef](#)]
12. Pouget, J.P.; Alemany, P.; Canadell, E. Donor-anion interactions in quarter-filled low-dimensional organic conductors. *Mater. Horiz.* **2018**, *5*, 590–640. [[CrossRef](#)]
13. Pouget, J.P.; Foury-Leylekian, P.; Bolloc'h, D.; Hennion, B.; Ravy, S.; Coulon, C.; Cardoso, V.; Moradpour, A. Neutron-scattering evidence for a spin-peierls ground state in (TMTTF)₂PF₆. *J. Low Temp. Phys.* **2006**, *142*, 147–152. [[CrossRef](#)]
14. Asada, M.; Nakamura, T. Magnetic resonance investigation for a possible antiferromagnetic subphase in (TMTTF)₂Br. *Phys. Rev. B* **2017**, *96*, 125120. [[CrossRef](#)]
15. Furukawa, K.; Hara, T.; Nakamura, T. Deuteration effect and possible origin of the charge-ordering transition of (TMTTF)₂X. *J. Phys. Soc. Jpn.* **2005**, *74*, 3288. [[CrossRef](#)]
16. Nad, F.; Monceau, P.; Nakamura, T.; Furukawa, K. The effect of deuteration on the transition into a charge ordered state of (TMTTF)₂X salts. *J. Phys. Condens. Matter* **2005**, *17*, L399–L406. [[CrossRef](#)]
17. Dumm, M.; Loidl, A.; Fravel, B.W.; Starkey, K.P.; Montgomery, L.K.; Dressel, M. Electron spin resonance studies on the organic linear-chain compounds (TMTCF)₂X (C = S, Se; X = PF₆, AsF₆, ClO₄, Br). *Phys. Rev. B* **2000**, *61*, 511–521. [[CrossRef](#)]
18. Salameh, B.; Yasin, S.; Dumm, M.; Untereiner, G.; Montgomery, L.; Dressel, M. Spin dynamics of the organic linear chain compounds (TMTTF)₂X (X = SbF₆, AsF₆, BF₄, ReO₄, and SCN). *Phys. Rev. B* **2011**, *83*, 205126. [[CrossRef](#)]
19. We cannot guarantee that the experiments have been conducted under exactly the same conditions. Cooling rates as well as heat transfer rates may have differed between the measurements on the deuterated and protonated crystals, which may influence the hysteresis of this transition.
20. Pouget, J.P.; Ravy, S. Structural aspects of the Bechgaard salts and related compounds. *J. Phys. I* **1996**, *6*, 1501–1525. [[CrossRef](#)]
21. Dumm, M.; Loidl, A.; Alavi, B.; Starkey, K.P.; Montgomery, L.K.; Dressel, M. Comprehensive ESR-Study of the Antiferromagnetic Ground States in the One-Dimensional Spin Systems (TMTSF)₂PF₆, (TMTSF)₂AsF₆, and (TMTTF)₂Br. *Phys. Rev. B* **2000**, *62*, 6512–6520. [[CrossRef](#)]
22. Tomić, S.; Biskup, N.; Dolamski Babić, S.; Maki, K. Commensurate Spin-Density Wave State in (TMTTF)₂Br: Single-Particle and Collective Charge Dynamics. *Europhys. Lett.* **1994**, *26*, 295–301. [[CrossRef](#)]

23. Baranovski, S. *Charge Transport in Disordered Solids with Applications in Electronics*; John Wiley & Sons: West Sussex, UK, 2006.
24. Mott, N.F.; Davies, E. *Electronic Processes in Non-Crystalline Materials*, 2nd ed.; Clarendon Press: Oxford, UK, 1979.
25. Efros, A.L.; Shklovskii, B.I. Coulomb gap and low temperature conductivity of disordered systems. *J. Phys. C* **1975**, *8*, L49. [[CrossRef](#)]
26. Shklovskii, B.I.; Efros, A.L. *Electronic Properties of Doped Semiconductors*; Springer: Berlin, Germany, 1984.
27. Khondaker, S.I.; Shlimak, I.S.; Nicholls, J.T.; Pepper, M.; Ritchie, D.A. Crossover phenomenon for two-dimensional hopping conductivity and density-of-states near the Fermi level. *Solid State Commun.* **1999**, *109*, 751. [[CrossRef](#)]
28. Strictly speaking $\gamma = 2$ is also obtained in the case of one-dimensional transport ($d = 1$). The thorough study of anisotropic transport reveals that at low-temperatures one-dimensional models do not apply despite the appreciable anisotropy.
29. Dressel, M.; Petukhov, K.; Salameh, B.; Zornoza, P.; Giamarchi, T. Scaling Behavior of the Longitudinal and Transverse Transport in Quasi One-Dimensional Organic Conductors. *Phys. Rev. B* **2005**, *71*, 075104. [[CrossRef](#)]
30. Joung, D.; Khondaker, S.I. Efros-Shklovskii variable range hopping in reduced graphene oxide sheets of varying carbon sp^2 fraction. *Phys. Rev. B* **2012**, *86*, 235423. [[CrossRef](#)]

Publisher's Note: MDPI stays neutral with regard to jurisdictional claims in published maps and institutional affiliations.



© 2020 by the authors. Licensee MDPI, Basel, Switzerland. This article is an open access article distributed under the terms and conditions of the Creative Commons Attribution (CC BY) license (<http://creativecommons.org/licenses/by/4.0/>).